On the true morphology of highly photoactive anatase TiO$_2$ nanocrystals

M. Čaplovičová [a,*], P. Billik [a,b], Ľ. Čaplovič [c], V. Brezová [d], T. Turáni [e], G. Plesch [a], P. Fejdi [a]

[a] Faculty of Natural Sciences, Comenius University, Mlynská Dolina, SK-842 15 Bratislava, Slovakia
[b] Department of Magnetometry, Institute of Measurement Science, Slovak Academy of Sciences, Dúbravská cesta 9, SK-841 04 Bratislava, Slovakia
[c] Institute of Materials Science, Faculty of Materials Science and Technology in Trnava, Slovak University of Technology in Bratislava, Paulínska 16, SK-917 24 Trnava, Slovakia
[d] Institute of Physical Chemistry and Chemical Physics, Faculty of Chemical and Food Technology, Slovak University of Technology in Bratislava, Radlinského 9, SK-812 37 Bratislava, Slovakia
[e] Kadaň Ltd., Lapášska cesta 458, 951 02 Pohranice, Slovakia

ABSTRACT

Nanosized titania photocatalysts were prepared from a TiOSO$_4$·2H$_2$O–Na$_2$CO$_3$ mixture via high-energy milling for 5 min, and subsequent annealing at a temperature range of 300–700 °C/1 h. Photoactivity of all samples monitored by electron paramagnetic resonance (EPR) spectroscopy was correlated with phase composition, crystallinity, crystal size and morphology of the annealed products. The anatase nanocrystals with an XRD average size of 24 nm and well-faceted bipyramidal morphology exposed mainly by {1 0 1} type planes obtained on heating at 700 °C, exhibited markedly higher photoactivity than the Aeroxide® P25 TiO$_2$ standard and sample annealed at 600 °C. The rapid increase in photoactivity was assigned to complete crystallization of the sample, optimal size, but mainly to the well-developed bipyramidal morphology of anatase nanocrystals and enlargement of the {1 0 1} type plane area due to final growth of bipyramids in the ⟨0 0 1⟩ direction.

The weak beam dark field (WBDF) transmission electron microscopy (TEM) method was used to characterize morphology of the nanocrystals. Based on the thickness changes along the electron beam incidence inside the individual nanocrystals yielded by WBDF images, it was demonstrated that the mixture of polyhedral shaped anatase projections, such as square-like, hexagonal-like, rhomboid-like, rhombic-like, and rectangular-like prevailing in bright-field (BF) images, corresponds exclusively to tetragonal bipyramidal shape projected along different crystallographic directions. WBDF images of the most often occurring anatase nanocrystal projections are summarized and compared with both the schematic depictions of similarly oriented anatase bipyramids and that recorded in BF images. The difficulties of 3D morphology assessment from the projected nanocrystal shapes are highlighted. Attention is paid to the determination of facets limiting the nanocrystals, using the high resolution (HR)TEM method.

© 2012 Elsevier B.V. All rights reserved.

1. Introduction

The basic principle of semiconductor photocatalysis involves the absorbtion of a photon which leads to electron (e$^-$) and positive hole (h$^+$) pair formation [1–3]. The resulting e$^-$–h$^+$ pairs can migrate towards the catalyst surface and initiate redox reactions in which adsorbed organic molecules are oxidized [4], or they may undergo undesirable recombination [1]. In order to prevent e$^-$–h$^+$ recombination, the highly active photocatalyst should have a high degree of crystallinity [5].

Since the heterogeneous photocatalytic reactions primarily take place on the catalyst surface [1–5], the surface structure (surface atomic arrangement) and area, and the kind and number of surface-active sites (surface atomic coordination), where the photogenerated charge-carriers can undergo interfacial transfer and react with adsorbed molecules are also critical in controlling the photocatalytic reactivity [6,7].

In this context, the nanoparticle size is an especially important parameter, since it directly affects the specific surface area of a catalyst [1], and thus the number of surface-active sites. Smaller particles are generally preferred for use as photocatalysts, because of their high specific surface area leading to a greater number of active surface sites. However, the photocatalytic activity does not increase monotonically with decreasing particle size, since the benefit from the high surface area is offset by a higher recombination rate of electron–hole pairs at the surfaces of the too-small nanoparticles [8–11]. The large surface area to afford a lot of active sites is also very significant in achieving of the high photocatalytic activity of the architectures with appropriate macro-/meso-porosity [12–15].

Recent experimental studies have shown that the density of catalytically active sites is also crystal plane dependent [16–20].

* Corresponding author. Tel.: +421 2 60296 269; fax: +421 2 60296 273.
  E-mail address: caplovicova@fns.uniba.sk (M. Čaplovičová).

Therefore, information on catalyst morphology and particularly on the type and abundance of the specific crystal facets exposed on the surfaces is of great importance [21]. Since the crystal facet engineering has become an important strategy for optimizing reactivity of photocatalysts, it is essential to understand how morphology, and especially specific surface facets, affects photocatalytic performance. However, it seems that the morphology–photoactivity relationship is not well understood, because some controversial conclusions on morphology of anatase, which is one of the most important photocatalysts, and thus on facets responsible for catalytic performance, have been reported.

In accordance with Density Functional Theory (DFT) calculations [16–20], anatase facets with a high percentage of under-coordinated five-fold Ti atoms (Ti_{5c}) possess superior reactivity to those with a low percentage of Ti_{5c} atoms. In this respect, the {1 0 1} facets that are most abundant on the surfaces of bipyramidal anatase nanocrystals, are considered to have low photoactivity since they possess only 50% Ti_{5c} atoms, while both highly reactive {0 0 1} and {1 0 0} type facets have 100% Ti_{5c} [16,18,19,21].

To prepare highly efficient anatase nanoparticles in accordance with DFT calculations, a great deal of effort was devoted to synthesizing nanocrystals faceted predominantly by {0 0 1} and {1 0 0} type planes. Nanosheets/nanoplates with a large percentage of exposed {0 0 1} facets were produced by a modified hydrothermal method using fluorine to stabilize the {0 0 1} facets [6,22–28]. In addition, both highly active anatase nanorods with dominating {1 0 0} type planes and a small amount of {1 0 1} and {0 0 1} surfaces creating the pyramidal termination [29–33], and nanocuboids wholly faceted by {1 0 0} and {0 0 1} facets [34,35] were prepared.

However, contrary to conventional acceptance, the anatase nanoparticles with bipyramidal morphology faceted predominantly by {1 0 1} type planes and exhibiting excellent photocatalytic behaviour were reported in [36–40]. Moreover, highly photoactive anatase nanorods with ⟨0 0 1⟩ growth axis and corrugated sides due to oscillatory repetition of (1 0 1) and (1 0 1̄) planes [41–43] and anatase nanobelts favoured by {1 0 1} facets have also been produced [9]. Since the {1 0 1} facets are the most abundant on these nano-objects, one can expect that the photoactivity will be largely determined by these surfaces [17]. Experimental results of Amano et al. [37] and Wu et al. [9] indicated that {1 0 1} surfaces can be effective for photocatalytic oxidative decomposition of organic compounds in the presence of molecular oxygen. On the other hand, it was also reported in [37] that these facets are not as effective as other surfaces exposed on ordinary anatase particles for H_2 evolution in the absence of molecular oxygen.

To clarify the discrepancy between the experimental results and DFT calculations, Posternak et al. [44] demonstrated that four-fold Ti–two-fold O (Ti_{4c}–O_{2c}) pairs of under-coordinated atoms on ridge edges delimited by differently oriented {1 0 1} surfaces of anatase play a major role in the observed high chemical activity. The possible influence of surface defects on the photocatalytic reactivity of {1 0 1} facets was also considered [17,38].

In contrast to conventional understanding, more recently, Pan et al. [39] reported a new photoreactivity order in the photooxidation and photoreduction reactions for generating hydroxyl radicals ($OH^•$) and hydrogen evolution for clean {0 0 1}, {1 0 1}, and {0 1 0} anatase facets as follows: {0 1 0} > {1 0 1} > {0 0 1}. According to these authors, not only surface atomic structures (the proportion of under-coordinated atoms on the surface) play a substantial role in photoreactivity of facets, but also surface electronic structures, which are very often neglected. In terms of surface Ti_{5c} atoms, both {0 0 1} and {0 1 0} would exhibit a higher photoreactivity than {1 0 1}. However, since the conduction band (CB) minimum for {0 0 1}, {1 0 1}, and {0 1 0} facets satisfies the order {1 0 1} ≈ {0 1 0} > {0 0 1}, conversely, {1 0 1} and {0 1 0} should have

superior photoreactivity to {0 0 1} when it is considered that more strongly reductive electrons can be generated on {1 0 1} and {0 1 0} facets with a higher CB minimum.

The higher photocatalytic reduction activity of {1 0 1} than {0 0 1} was also validated by probing the single molecule fluorescence burst on anatase single-crystals [45] and by the selective metal deposition method [38].

Although, numerous studies have been devoted to the characterization of photoactivity-morphology relationship of anatase photocatalysts so far [22–31, 46–52, etc.], to the best of our knowledge, only few papers have been published where the high photoactivity of anatase was related to the tetragonal bipyramidal morphology favoured by {1 0 1} type planes [36–40]. This may be affected by the fact that the morphology of highly photoactive bipyramidal/truncated bipyramidal anatase nanocrystals can be misinterpreted, as they were often considered to be cuboidal/rectangular nanoplates [43,53], quasi-cubic nanoparticles [54], polyhedral (cubic and hexagonal) nanoparticles [55–57], truncated octahedral/cubooctahedral nanoplates [58], and rhombic-shaped nanoplates with a large percentage of exposed {0 1 0} facets [59–61], etc.

To provide conclusive evidence for this assertion, the detailed morphological study of bipyramidal anatase nanocrystals using WBDF images depicting the projected thickness of the crystals is demonstrated herein. To the best of our knowledge, this is the first report on the 3D morphology characterization of anatase photocatalyst using the WBDF method. Therefore, the WBDF morphology characterization is provided in detail, and possible misleading interpretations are highlighted. The objective of this paper is also to characterize the fundamental processes of nucleation, growth and well-faceted morphology evolution using bright-field (BF), dark-field (DF), high-resolution transmission electron microscopy (HRTEM), and selected area electron diffraction (SAED) techniques and, based on the gained results, to perform comprehensive analysis of the structural-morphology–photoactivity relationship on the produced TiO_2 photocatalyst.

2. Experimental

The mechano-chemical synthesis of titania powders was performed in the high-energy planetary mill TB-1 (Kadaň Ltd., Slovakia). The starting materials were $TiOSO_4 \cdot 2H_2O$ (Riedel-de Häen) and Na_2CO_3 powders (Lachema). Before milling, the free H_2O and H_2SO_4 in the commercial $TiOSO_4 \cdot xH_2O \cdot yH_2SO_4$ powder were eliminated by washing with ethanol. Corundum balls of 10 mm diameter with a weight of 100 g, and corundum jars with 0.3 dm³ inner volume were used. Milling was performed for 5 min using a ball to powder mass ratio of 10:1, and the milling speed was fixed at 890 rpm. The powders were prepared with a $TiOSO_4 \cdot 2H_2O/Na_2CO_3$ molar ratio of 1:1. These prepared products were annealed in air over a temperature range of 300–700 °C for 1 h. The $Na_2SO_4 \cdot xH_2O$ water-soluble byproduct salt matrix was then removed by washing with distilled water using an ultrasonic bath for 1 min, and it was filtered, washed and dried at 200 °C for 1 h under air. The more detailed description of mechano-chemical synthesis of catalyst nanoparticles is given in [62,63].

The phase composition of the prepared powders was examined with a Philips PW 1050 diffractometer using Cu Kα radiation. The fraction of the crystalline phase ⟨F_c⟩ in the powder was evaluated using the relative integral intensity of the diffraction peak corresponding to the {1 0 1} planes [64]. Crystallite sizes (D) were calculated by X-ray line broadening using the Scherrer's equation, as follows [63]:

$$D = \frac{0.9\lambda}{B\cos\theta} \quad B^2 = B^2 - B^2 \tag{1}$$

where D is the crystallite size, λ the wavelength of the X-ray radiation (0.15418 nm), B_s is the full width at half-maximum height (FWHM) of the 1 0 1 anatase diffraction peak of the sample in radians, and θ is the diffraction peak position of the sample. For the correction of the instrumental peak-broadening (B_m), the 012 diffraction of the α-Al_2O_3 standard calcined at 1500 °C was used [65].

In order to study the precrystallization of the as-milled powder and also the size and morphology of the grown nanocrystals, the BF, DF, WBDF, selected area electron diffraction (SAED), and HRTEM methods were employed. TEM analysis was performed on the TEM JEOL 2000FX device working at the accelerating voltages of 160 kV and 200 kV.

Samples for TEM examination were prepared by deposition of a drop of strongly diluted suspension consisting of produced powders and ethanol on a holey-carbon-coated Cu-grid. After drying in air, the samples were examined by TEM.

The photo-induced activity of synthesized anatase nanopowders was measured using electron paramagnetic resonance (EPR) spectroscopy (Bruker EMX EPR spectrometer) monitoring in situ the termination of the EPR signal of 1,1-diphenyl-2-picrylhydrazyl (DPPH; Fluka) free radical [66]. The concentration of DPPH stock solution in ethanol (Mikrochem; spectroscopic grade) was 100 μmol dm^{-3}. The TiO_2 suspensions (water:ethanol = 1:1; v/v; 0.5 g TiO_2 dm^{-3}) containing DPPH (50 μmol dm^{-3}) were irradiated at 293 K directly in the EPR spectrometer resonator using a small quartz flat cell (WG 808-Q, Wilmad-LabGlass, USA), and the EPR spectra were recorded in situ. As an irradiation source a HPA 400/30S lamp (400 W, Philips) was used (irradiance of 5 mW cm^{-2} at 365 nm). A Pyrex glass filter was used to eliminate radiation wavelengths below 300 nm. Upon UVA irradiation of aerated TiO_2 suspensions in the presence of DPPH, the decrease in intensity of the typical five-line EPR spectrum (a_{N1} = 0.927 mT, a_{N2} = 0.846 mT; g = 2.0036) was monitored. The experimental dependencies of DPPH concentration on irradiation time were fitted by the nonlinear least-squares method to the formal first-order kinetic model, and the formal initial rate of DPPH termination R_{in} (DPPH) was calculated. More detailed technical information is contained in [40,67].

3. Results and discussion

3.1. Microstructural characterization of produced TiO_2 powder samples

All of the samples investigated were prepared by mechanochemical synthesis from $TiOSO_4 \cdot 2H_2O$ and Na_2CO_3 reactants according to the previously described procedure [62].

It can be concluded from XRD measurements [63] that the mechano-chemical treatment for 5 min led to a powder mixture of $Na_2SO_4 \cdot xH_2O$ salt matrix and amorphous titania according to the following reaction:

$$TiOSO_4 \cdot 2H_2O + Na_2CO_3 \rightarrow TiO_2 \cdot xH_2O + Na_2SO_4 \cdot xH_2O + CO_2$$

(1)
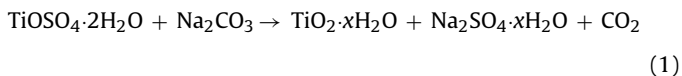
After the $Na_2SO_4 \cdot xH_2O$ salt matrix was removed by washing, only amorphous titania was revealed in the samples. The gradual transformation of amorphous titania to anatase nanocrystal occurred on heating at temperatures of 300–700 °C, and microstructural changes in the individual powders dependent on crystallinity, size and morphology of evolved nanocrystals were estimated by TEM.

Fig. 1(a) shows a typical low magnification BF image of the as-prepared TiO_2 powder sample upon washing. TiO_2 powders with sizes of 50–400 nm appear as shapeless single-phase features.

Table 1
Average crystal size of anatase (d) and percentage of crystalline phase (Fc) in titania powders prepared by annealing in temperature range 300–700 °C determined by XRD method.

| Annealing temperature (°C)	Average XRD anatase nanocrystal size (d)	Fraction of crystalline phase $\langle F_c \rangle$
300	~2	~0.20
400	6	0.64
500	12	0.93
600	20	0.97
700	24	1.00

However, many fine bright spots observed in DF image, Fig. 1(b), indicate the presence of tiny domains of coherent scattering in the amorphous TiO_2 matrix. The presence of fine diffracting domains is evident also from the intensity profile (bottom inset in Fig. 1(a)), recorded from relevant SAED circles. The d_{hkl} values (0.35 nm, 0.192 nm and 0.172 nm) estimated from intensity profile match the interlayer spacings of the strongest anatase reflections 101, 200 and 105 (JCPDS 21-1272). The more detailed HRTEM image in the upper inset of Fig. 1(b) shows anatase nanocrystallite embedded in amorphous titania and the lattice fringes spaced at 0.35 nm can be assigned to the {1 0 1} type planes. The influence of the electron beam on the generation of fine anatase domains in the amorphous TiO_2 matrix during TEM examination can be excluded, since their presence was also confirmed by XRD measurement (inset in Fig. 1(b)). The strongest anatase reflection 101 and the broad reflection corresponding to the {1 0 5} and {2 1 1} planes are arrowed in this image. It was proven that in contrast to the commonly used preparation routes in which pre-prepared less crystalline TiO_2 particles or nanostructured titanataes as precursors are used to generate anatase nanoparticles [37,45,47], the high-energy milling of $TiOSO_4 \cdot 2H_2O$ and Na_2CO_3 reactants led to the formation of tiny anatase domains serving as precursors of anatase nanocrystals.

With calcinations at a temperature range of 300–600 °C, the amorphous titania progressively transformed into anatase, Table 1. While anatase nanocrystals with average sizes of 2 nm and 6 nm were evolved in the amorphous matrix of the pristine particles when heated at 300 °C and 400 °C, rising the calcination temperature above 500 °C led to marked disintegration of the original titania powders. BF, DF and HRTEM images of the powder samples upon calcination at 500 °C and 600 °C, where dispersed single crystals with an average size of 12 nm and 20 nm are depicted, are summarized in Fig. 2(a–f) and in Table 1. Relevant SAED patterns are indicative of anatase phase, and the most intensive circles belong exclusively to the 101, 004, 200 and 105 diffractions.

The transformation of amorphous titania was completed at 700 °C, where exclusively pure anatase nanocrystals were revealed in the sample (Fig. 2(g–i)). As determined by measurement of 200 nanocrystals depicted in TEM images, their sizes ranged from 15 to 40 nm. For comparison, the average size of 24 nm was determined by XRD method (Table 1). No traces of the rutile phase were found in the sample either by SAED (Fig. 2(g)) or by XRD methods [62]. Fig. 2(g) and (h) manifest the mixture of different nanocrystal shapes, mainly rectangular-like, hexagonal-like, square-like, rhombic-like, and rhomboid-like. It must be noted that patterns observable in TEM images are not true shapes of crystals but only the corresponding two-dimensional (2D) projections.

The more detailed HRTEM images in Fig. 2(c), (f), and (i) revealed a gradual evolution of anatase morphology during annealing at a temperature range of 500–700 °C. As apparent in the comparison of these images, most of the nanocrystals grown at 500 °C and 600 °C were isometric/isometric partly faceted without striking preferential growth. Apparently, the well-faceted anatase shapes generated due to enhanced growth in the $\langle 0\,0\,1 \rangle$ direction, were
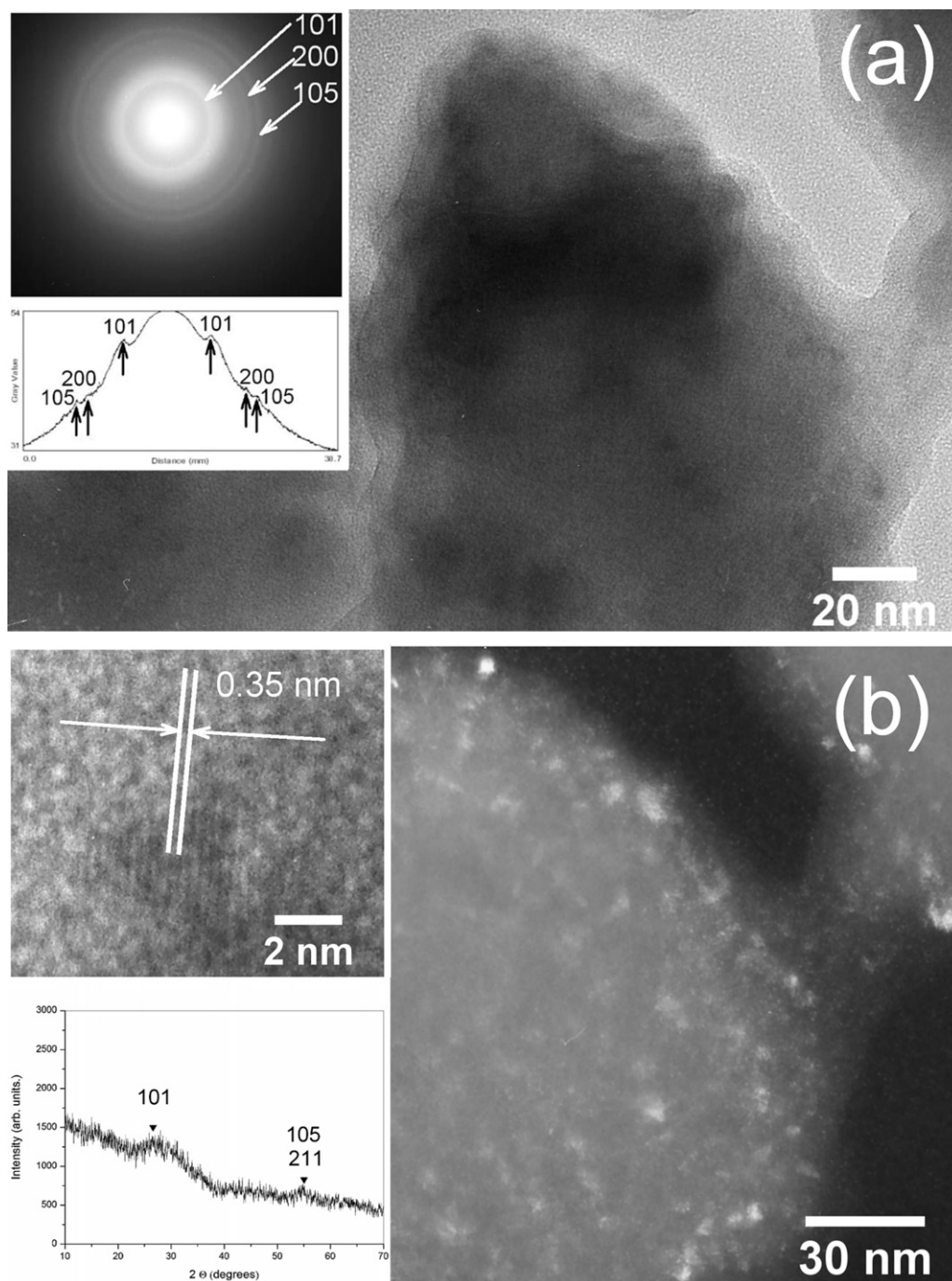
Fig. 1. As-milled TiO$_2$ sample. (a) BF TEM image with SAED pattern in the upper inset and intensity profile in the lower inset. (b) DF TEM image with XRD pattern in inset.

evolved on calcination at 700 °C, Fig. 2(i). As is shown in Fig. 2(i) and (f), two strongly faceted edges parallel to lattice fringes spaced at 0.35 nm are the {1 0 1} type planes of anatase. The [0 0 1] direction is highlighted in these images in accordance with the anatase crystal structure, where the angle of 68.304° coincides with that between the {0 0 1} and {1 0 1} type faces. As can be seen in Fig. 2(i), during the growth in the [0 0 1] direction at 700 °C, the area of the {1 0 1} type planes exposing the bipyramids was increased compared with the nanocrystals formed at 600 °C (Fig. 2(f)). This result coincides with that reported in [27,36]. Moreover, the HRTEM image in Fig. 2(i) confirms that anatase single crystals grown at 700 °C exhibit high crystallinity and no an amorphous phase on the surface.

3.2. Morphological characterization of evolved anatase nanocrystals

Since conventional BF images yield only a two-dimensional (2D) projection of a three-dimensional (3D) object, it is difficult to recognize the true 3D shapes of the crystals [68,69]. In order to avoid misinterpretation, the WBDF method, as well as HRTEM and BF methods, was used herein to determine the true 3D shape and faceting of the produced anatase catalyst.

The WBDF technique utilizes the weak beam diffracted by the crystals in the off-Bragg conditions [68,69] and yields the view of a crystal in terms of its thickness (the thickness maps). Crystals, which satisfy the Bragg diffraction condition would have DF images
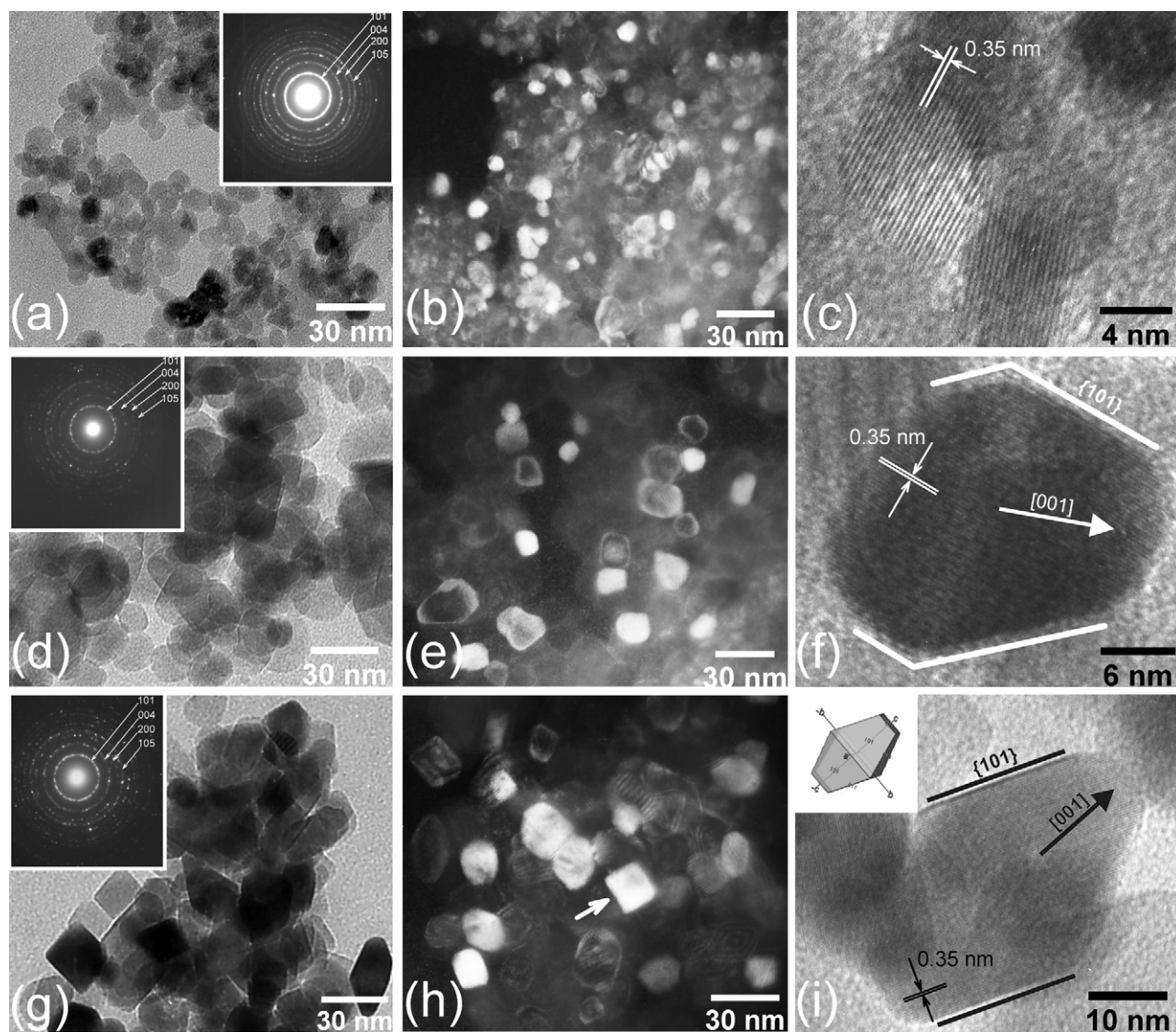
Fig. 2. Morphology evolution of anatase nanocrystals as a function of calcination temperature. BF with SAED pattern, DF and HRTEM images of anatase nanocrystals evolved (a–c) at 500 °C/1 h, (d–f) at 600 °C/1 h, and (g–i) at 700 °C/1 h, respectively. (i) HRTEM image of truncated bipyramid close to ⟨0 1 0⟩ projection.

with uniform contrast (as is arrowed in Fig. 2(h)), while the crystals out of the Bragg diffraction condition, as in the WBDF technique, exhibit alternating bright and dark fringes, Fig. 3(a2–h2) . Each fringe in the WBDF images represents an equal thickness area in the crystal. The distribution of the thickness fringes varies depending upon the angle, from which the crystal is viewed, Fig. 3(a2–h2). The larger the tilt from the Bragg condition results in a greater number of thickness fringes [69].

Upon annealing at 700 °C, the high heterogeneity in shapes in the BF images was observed, Fig. 2(g), and most nanocrystals possessed well-faceted polyhedral shapes, mainly with square-like, rectangle-like, hexagonal-like, rhombic-like, and rhomboid-like 2D projections. Keeping in mind that these patterns are not the true shapes of crystals, it is necessary to determine whether all these patterns correspond to a single shape projected along different crystallographic directions, or to more crystal shapes. To solve this problem, the 2D shapes of anatase obtained by the BF method (Fig. 3 (a1–h1)) are compared both with the relevant WBDF images (Fig. 3(a2–h2)) and with the schematic representation of the truncated tetragonal bipyramids of anatase nanocrystal oriented approximately in the same direction as the depicted nanocrystals, Fig. 3(a3–h3) [70].

In general, square-like 2D projections can exhibit both cuboidal and tetragonal pyramidal/bipyramidal nanocrystals oriented in the [0 0 1] direction parallel to the incident electron beam. While cuboids, which have equal dimensions along the ⟨0 0 1⟩ directions, would lead to uniform contrast without fringes in WBDF images [68], tetragonal pyramidal/bipyramidal forms would contain the equal-thickness fringes parallel to the edges of the square-like feature in WBDF images. This is due to thickness variation along the electron beam incidence. Since the equal-thickness fringes parallel to the edges of the square-like form were revealed inside the nanocrystals in the WBDF images, as seen in Fig. 3(a2), the tetragonal pyramidal/bipyramidal morphology of anatase exhibiting the ⟨0 0 1⟩ direction parallel to the electron beam was confirmed. The small square-like area exhibiting uniform contrast (without fringes) at the centre of nanocrystal in Fig. 3(a2) displays the top of a truncated bipyramid where constant thickness along the electron beam incidence is expected. The thickness fringe distribution inside the nanocrystal taken in Fig. 3(b2) suggests that the slightly tilted tetragonal bipyramid is depicted herein, and this is in accordance with the scheme in Fig. 3(b3). Similarly, all plate-/sheet-like forms with equal dimension along the electron beam incidence, should exhibit uniform contrast in WBDF images.

However, the presence of the thickness fringes inside the studied 2D shapes indicated that nanocrystals are not flat, but they exhibit thickness variation, Fig. 3(a2–h2). Since nanocrystals with the uniform thickness contrast in WBDF images were not found in the sample, the platelet-/sheet-like shapes of anatase were excluded from further consideration. It is apparent from comparison of Fig. 3(c1–h1), (c2–h2), and (c3–h3) that all hexagonal-like, truncated rhombic-like, rhomboid-like, and rectangle-like 2D projections can also be attributed to bipyramidal morphology. The different distribution of thickness fringes depicted in the WBDF
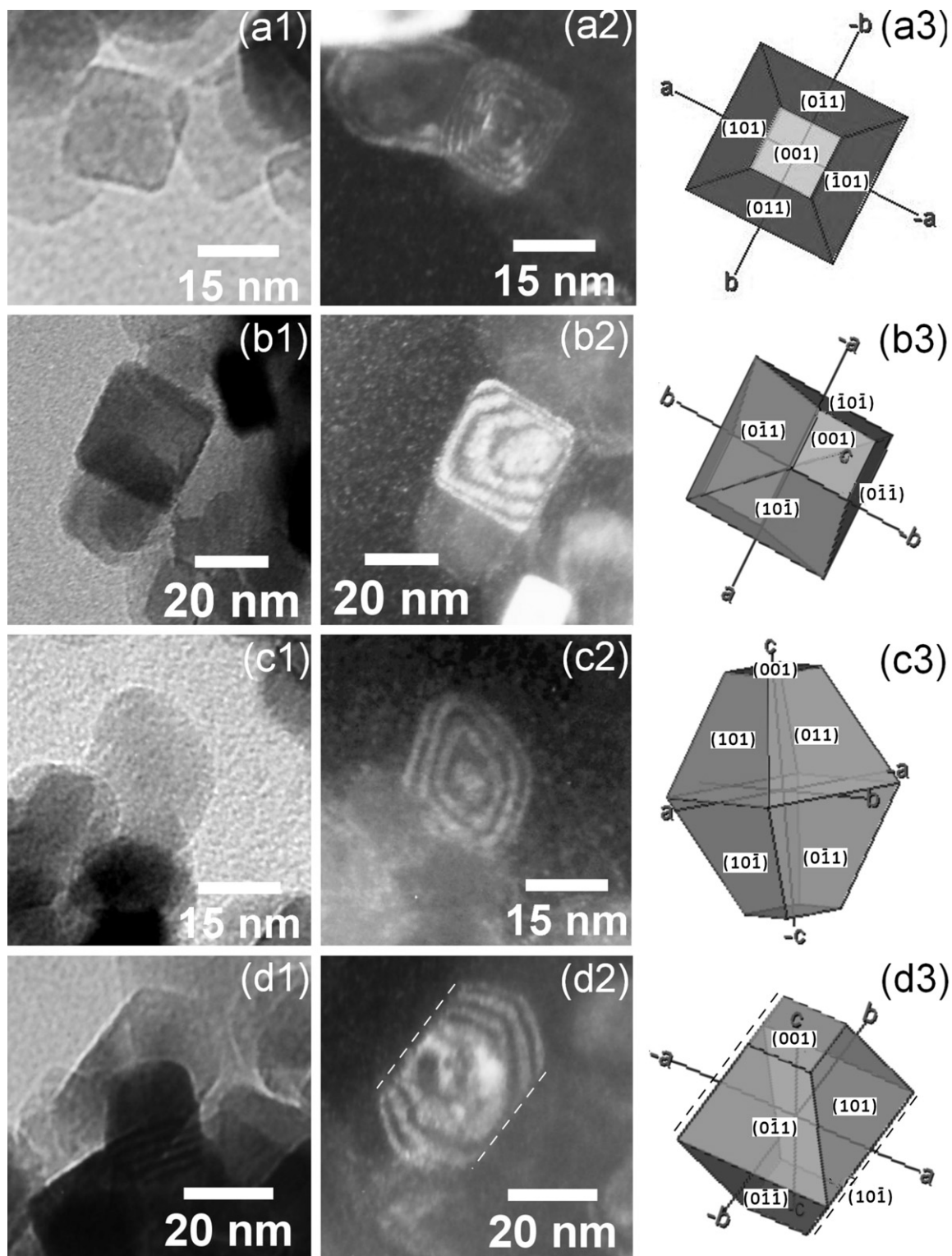
Fig. 3. The BF and WBDF images of the predominant 2D projections of anatase nanocrystals grown at 700 °C, and relevant schematic drawing of similarly oriented bipyramidal anatase nanocrystals. BF, WBDF images and scheme of anatase bipyramid exhibiting (a1–a3) square-like, (b1–b3) rhomb-like, (c1–c3) truncated rhomb-like, (d1–d3) and (e1–e3) quasi-hexagonal, (f1–f3) truncated rhomb-like projection close to ⟨0 1 0⟩ orientation, (g1–g3) rhomboid-like, and (h1–h3) rectangle-like 2D projections. Dashed lines both in WBDF images and in sketches of bipyramids mark respective the {1 0 1} type planes parallel to primary electron beam that enclose the tetragonal bipyramids.
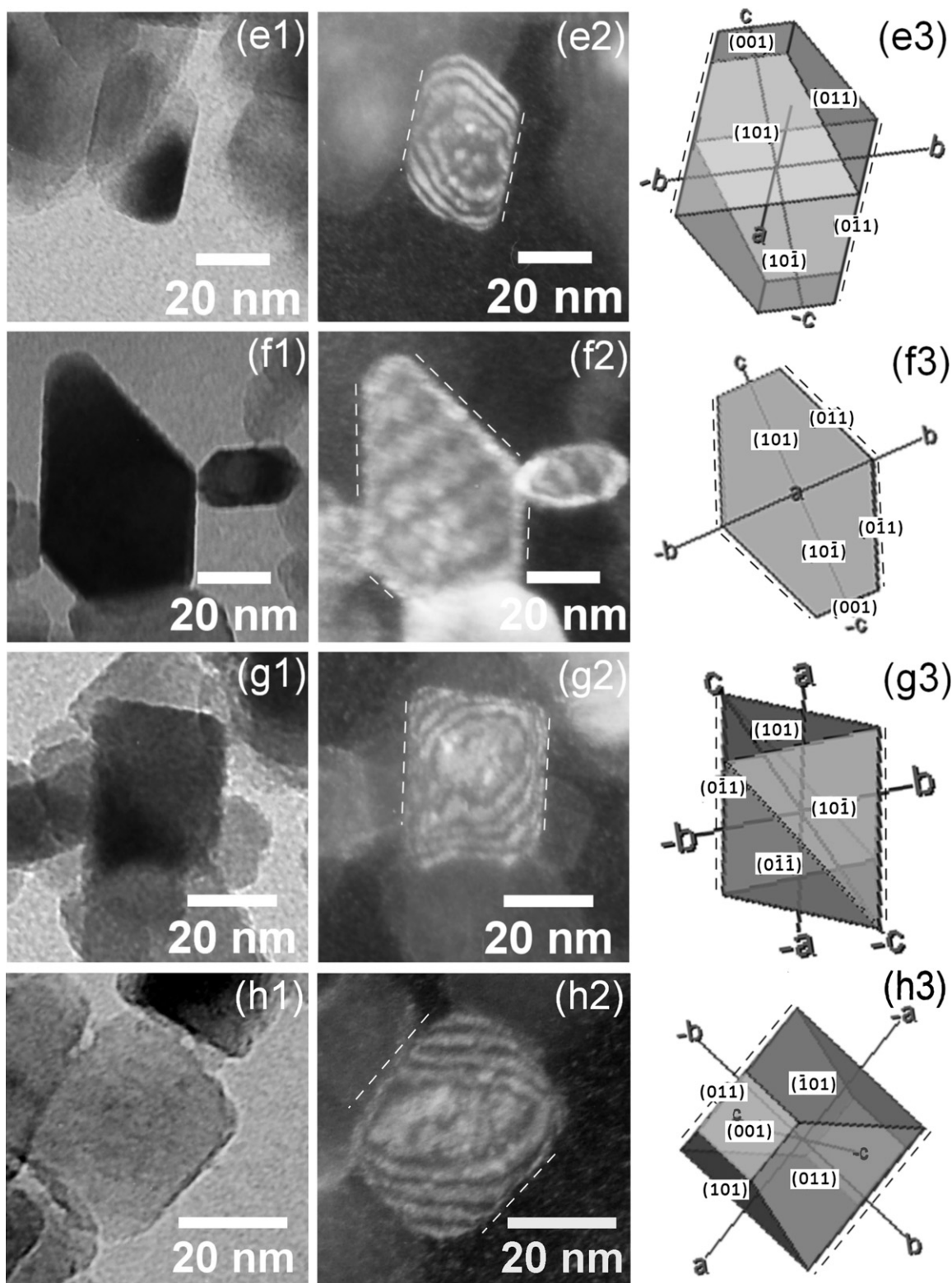
Fig. 3. (*continued*).

images which is usually observed from the periphery to centre of the nanocrystals depends on the viewing direction of the bipyramidal nanocrystals and maps the thickness variation along electron beam incidence, Fig. 3(c2–h2). The regions exhibiting uniform thickness without fringes are the thickest regions of the nanocrystals along the electron beam incidence, as follows from comparison of Fig. 3(c2–h2) and (c3–h3). The images in Fig. 3(a2–f2) and (h2) indicate that the produced anatase nanocrystals are slightly truncated bipyramids. On the other hand, the rhomboid-like feature in Fig. 3(g1) and (g2) manifests the presence of an acute anatase bipyramid. Therefore, it is proposed that the morphology of produced nanocrystals is changeable from bipyramids to slightly truncated bipyramids. The dashed lines in both the WBDF images and in corresponding schemes highlight the {1 0 1} type planes
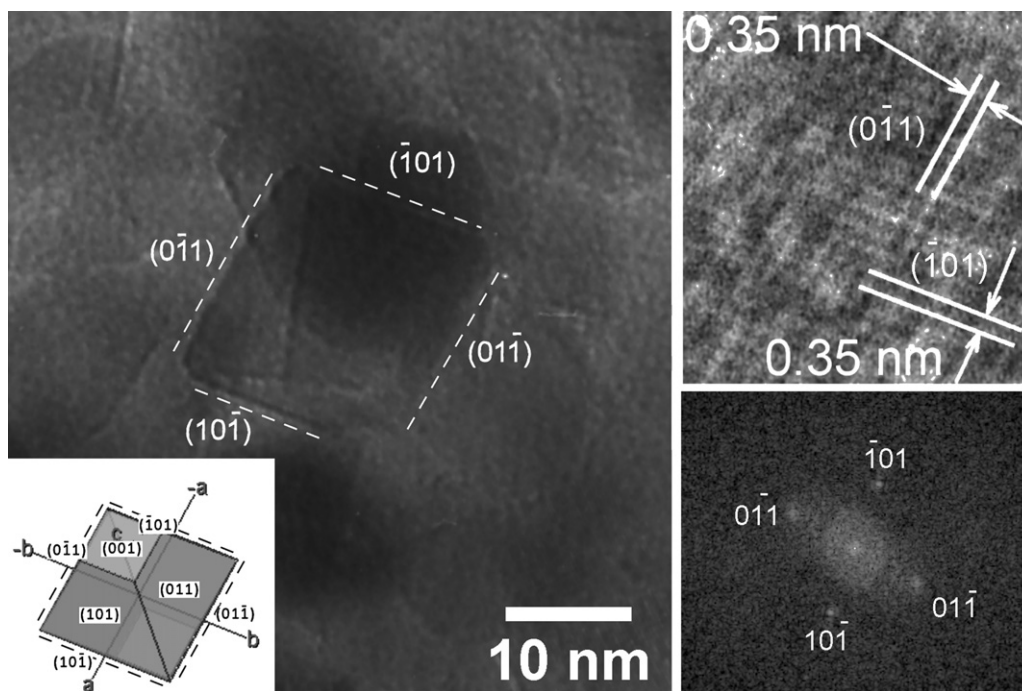
Fig. 4. BF image of anatase nanoparticle exhibiting rhomb-like 2D shape. The HRTEM image in the upper inset shows crossing lattice fringes 0.35 nm apart parallel to nanoparticle surfaces. The relevant FFT pattern is in the bottom inset. The labels show one of the possible ways of evaluating the surface facets and the orientation of the crystal.

parallel to the primary electron beam enclosing the nanocrystals.

From all the above, it can be concluded that all the aforementioned BF 2D projections depicted in Fig. 3(a1–h1) are related exclusively to the tetragonal bipyramids, and the projected shapes vary depending on the angle from which the nanocrystals are viewed.

Since the crystallographic facets exposed on the surfaces cannot be identified explicitly using the WBDF technique, but only deduced from relevant schematic drawings, the HRTEM method was employed for surface plane and crystal orientation assessment. The HRTEM images of the rhombic-/truncated rhombic-like, hexagonal-like and rectangle-/square-like projections of anatase are studied in detail, because anatase nanocrystals
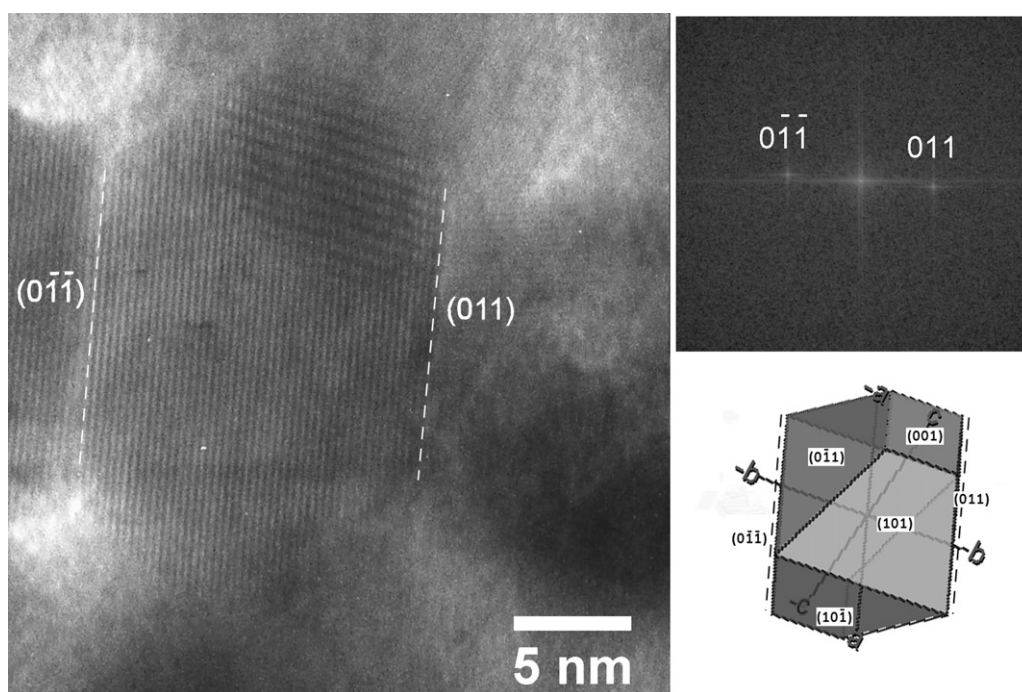
Fig. 5. HRTEM image of anatase nanocrystal with hexagonal-like projection. The well-faceted sides parallel to lattice fringes spaced at 0.35 nm are planes of the {1 0 1} type. The relevant FFT image and schematic representation of a similarly oriented tetragonal bipyramid are in the relevant insets. The labels show one of the possible ways of interpreting the FFT image and {1 0 1} type facets distribution on the surface of nanocrystal.
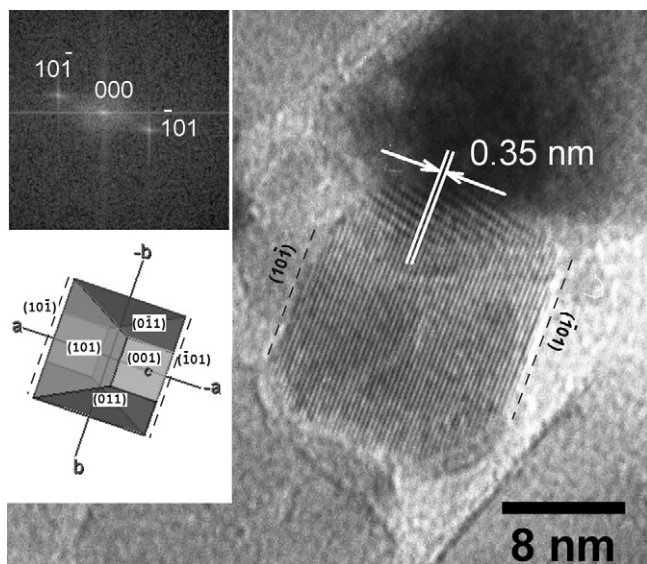
Fig. 6. HRTEM image of rectangle-like shape 2D projection of anatase single crystal. Well-faceted sides parallel to lattice fringes spaced 0.35 nm apart are {1 0 1} type planes. The relevant FFT pattern is in the upper inset. Truncated bipyramid presented by 3D scheme (in bottom inset) is oriented similarly to the anatase nanocrystal. The labels show one of the possible ways of interpreting the FFT image and {1 0 1} type facets distribution on the surface of nanocrystal.

Fig. 7. Initial rates of DPPH termination evaluated for titania samples synthesized at temperatures 300–700 °C and for Aeroxide® P25, along with data found in titania-free solutions (Reference). Inset represents an EPR spectrum of DPPH in water:ethanol (1:1; v/v; magnetic field sweep width 10 mT).

exhibiting similar outlines were often considered to be of plate-/sheet-like and cuboidal morphologies [53–55,58].

The well-faceted rhombic-like 2D projection of the anatase nanocrystal is arrowed in Fig. 4, and for comparison, the schematic depiction of a similarly oriented tetragonal bipyramid is in the bottom left inset. As follows from the HRTEM image in the upper right inset and the relevant FFT calculated diffractogram below, the measured angles of 82.2° and 97.8°, respectively, coincide with those of the theoretical values between the {1 0 1} type planes of anatase. The facets are crystallographically equivalent and the shape shown in this image represents a projection of a tetragonal bipyramid close to the [1 1 6] direction, as determined by the stereographic projection constructed for the anatase phase [71]. The dashed lines in both the BF image and in the sketch of a similarly oriented bipyramid mark the {1 0 1} type surface planes parallel to the primary electron beam. It can be concluded from this image that the nanocrystal is predominantly faceted by {1 0 1} type planes.

It should be noted that in agreement with the stereographic projection of crystals with 4/*mmm* point group symmetry in which anatase crystallizes, the {1 0 1} planes are pyramidal and therefore they facet only tetragonal pyramids/bipyramids. Furthermore, cuboidal-like anatase nanocrystals [6,22,53,54] cannot have dominant {1 0 1} surfaces, but the {1 0 0} or/and {0 0 1} type planes predominate. In the case that {1 0 1} type facets bind the rod-like objects, they cannot create flat, smooth surfaces, but these surfaces consist of inclined {1 0 1} planes [41–43].

HRTEM images of truncated rhombic-like, hexagonal-like, and truncated rectangle-like anatase single crystals are shown in Figs. 2(i), 5, and 6. The two well-faceted external surfaces marked by dashed lines parallel to the lattice fringes spaced 0.35 nm apart are {1 0 1} type facets, as determined by the FFT processing provided in the corresponding images. Other fuzzy facets cannot be positively determined from these images because of the tilting of nanocrystals away from an advantageous zone axis. However, faceting of the nanocrystals by pyramidal {1 0 1} type planes, and comparison with schematic drawing of the tetragonal bipyramid oriented approximately in the same direction as the depicted single crystals
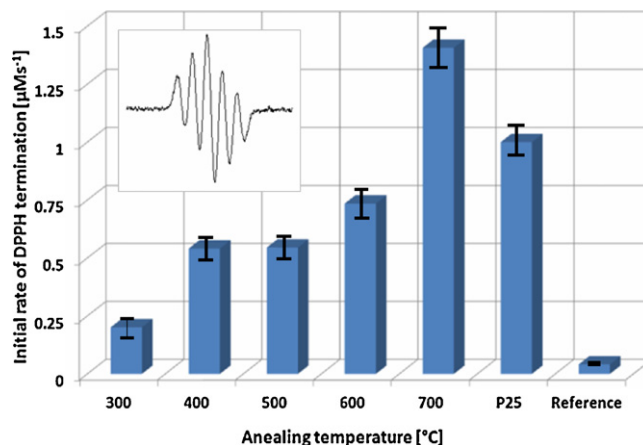
(as seen in respective insets), enabled us to conclude that anatase nanocrystals are in fact of tetragonal bipyramidal shape.

3.3. Photoactivity of produced anatase nanoparticles

The photocatalytic activity of TiO_2 is based on photoinduced generation of holes (h^+) and electrons (e^-), which reactions with molecular oxygen and surface H_2O/OH^- lead to the formation of reactive oxygen species (e.g., $^\bullet OH$, $O_2^{\bullet-}/^\bullet OOH$, H_2O_2, $^1O_2$) with high potential to decompose a wide range of organic substrates in aerated aqueous media [3,4,72,73]. The photoproduced reactive radical intermediates can be evidenced using the indirect methods of EPR spectroscopy, e.g., spin trapping technique or elimination of semi-stable free radicals added into photoactive heterogeneous TiO_2 systems [29,66,67]. It has been shown that the semi-stable DPPH radical can be effectively terminated by an electron transfer reaction, and by hydroxyl radical attack, which leads to transformation of paramagnetic DPPH to the diamagnetic products. The loss of DPPH paramagnetism can be easily monitored using the EPR method [74] and the termination of paramagnetic DPPH via photo-generated charge carriers upon photoexcitation of TiO_2 represents a suitable experimental technique for characterization of TiO_2 photoactivity [75–78]. The decrease in DPPH concentration upon UVA irradiation in aerated TiO_2 suspensions can be described by formal first-order kinetics, allowing calculation of the initial rate of DPPH termination, ($R_{in}(DPPH)$).

Fig. 7 summarizes the values of $R_{in}(DPPH)$ after UVA irradiation of DPPH in the presence of anatase nanocrystals heated at temperatures of 300–700 °C, the TiO_2 standard Aeroxide® P25, and the TiO_2-free water:ethanol (1:1; v/v) solutions. The obtained values of $R_{in}(DPPH)$ serve as a comparison of the ability to terminate the EPR signal of DPPH upon irradiation of individual synthesized titania samples and Aeroxide® P25 in aerated suspensions. The changes in photoactivity of synthesized titania samples evaluated from the DPPH radical termination are in good correlation with those acquired using EPR spin trapping technique [40].

3.4. Microstructure-morphology–photoactivity relationship

As clearly seen in Fig. 7, the photoactivity of as-milled TiO_2 powders progressively increases with a rising calcination temperature up to 400 °C, the independence of photoactivity on heating can be registered in the temperature range of 400–500 °C
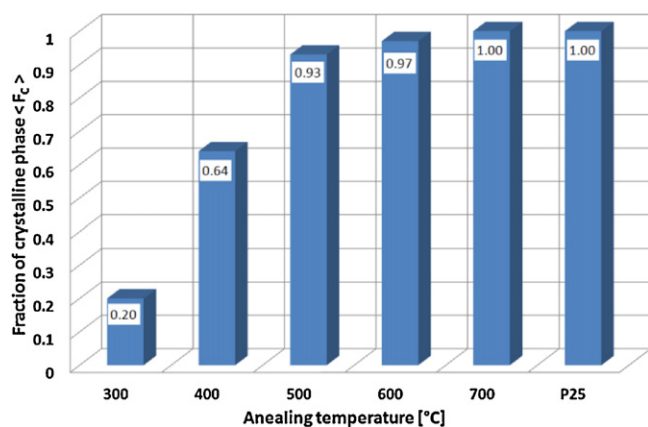
Fig. 8. Fractions of crystalline phase (F_c) in the produced anatase catalysts prepared by annealing at 300 °C, 400 °C, 500 °C, 600 °C, and 700 °C. For comparison, fraction of crystalline phase in TiO$_2$ standard Aeroxide® P25 is provided.

and rapid increase in the photoactivity occurred in the range of 600–700 °C. The result is that the sample calcined at 700 °C exhibited much higher photoactivity than the anatase sample annealed at 600 °C and the Aeroxide® P25 TiO$_2$ standard. The dependence of the photoactivity on the annealing temperature reflects the changes in crystallinity (Fig. 8), in size (Fig. 9) and in the morphology of evolved anatase nanocrystals in measured samples (Fig. 2(a–i)).

The as-milled TiO$_2$ sample consisted of powders sized in the range of 50–400 nm, which were created by fine crystalline domains of anatase embedded in amorphous titania, as demonstrated in Fig. 1(b). Upon annealing at 300 °C, the anatase nanocrystallites evolved in the particles, which maintained their original size and predominantly amorphous microstructure were 2 nm in size (Fig. 9). Since these mixed-phase particles consisted predominantly of highly defective amorphous titania (F_c ~0.2), which can be the recombination centre of photogenerated electrons and photogenerated holes [7,69], the sample exhibits the low photoactivity, Fig. 7.

The thermal treatment at 400 °C led to marked crystallinity improvement (Fig. 8), crystal growth to 6 nm (Fig. 9) and to a significant increase in photoactivity compared to the sample annealed at 300 °C, Fig. 7. The increment of photoactivity in this stage may be explained by the increasing fraction of
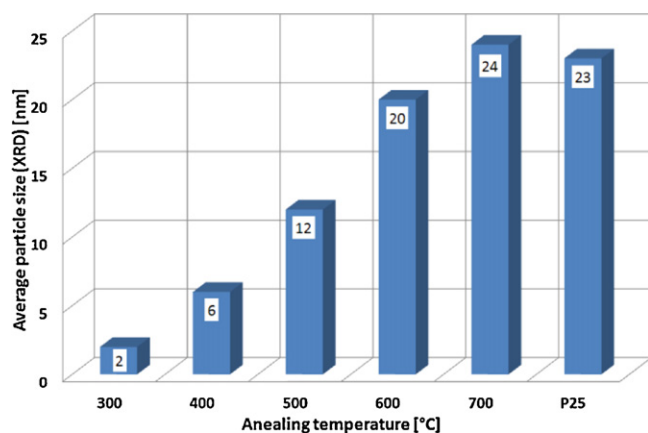
anatase phase, consuming the amorphous titania that is almost inactive in photocatalysis. It is expected that nucleation predominated over the growth, because many nanocrystallites exhibiting only a moderate growth were registered in the amorphous matrix of original particles after annealing at 400 °C, Fig. 9.

Further significant improvement in crystallinity of the sample due to continuing transformation of the amorphous phase, the complete breakdown of the mother particles to individual monodisperse spheroids and their growth to average size of 12 nm (Figs. 8, 9 and 2(a–c)) were registered after heating at 500 °C. However, as is demonstrated in Fig. 7, above given factors did not bring about a rise in photoactivity compared to the sample annealed at 400 °C. As follows from Fig. 9, the photoactivity was nearly independent of the size of anatase nanocrystals. In accordance with Cho et al. [36], the independence of photoactivity on the size of well-crystalline anatase nanocrystals exhibiting spherical-like morphology (Fig. 2(a–c)) in this growth stage can be clarified by the lack of faceting by the {1 0 1} type crystal planes. This our conclusion correlates well with the fact that annealing at 600 °C that led to the partial faceting of the produced anatase nanocrystals by the {1 0 1} planes (Fig. 2(d–f)), to the remarkable growth up to an average size of 20 nm (Fig. 9), and to further crystallinity improvement, Fig. 8, gave rise to the moderate increase in photoactivity. HRTEM image yielding the evidence of the anatase single crystal exhibiting partial faceting generated on annealing at 600 °C is in Fig. 2(f). Since the subtle crystallinity improvement and the moderate growth of nanocrystals were registered in this sample, it is proposed that partial faceting by the {1 0 1} type planes (Fig. 2(d–f)) can be primarily responsible for the moderate increment in photoactivity of evolved nanocrystals. This conclusion correlates with [55], where it was demonstrated that the dominant morphology of the nanocrystals is spherical in the less active catalysts, while polyhedral shapes preponderated in the samples with superior photocatalytic activity. The strong morphology influence on photoactivity presented herein correlates also with [9]. Wu et al. [9] have reported that single-crystalline anatase TiO$_2$ nanobelts exhibited enhanced photocatalytic activity over the nanosphere counterparts with an identical crystal phase and similar specific surface area.

As follows from Fig. 8, heating the samples resulted in rapid crystallization of amorphous titania and above 500 °C the samples were almost fully crystalline. Similar finding was reported in [79]. Based on this image, it is expected that the nanocrystal size increase at temperatures above 500 °C may be predominantly related to coalescence events and the crystallinity improvement may be mainly related to elimination of the lattice defects present in the evolved anatase nanocrystals.

Heat treatment at 700 °C resulted in sample consisting of anatase nanocrystals possessing high crystallinity. The transformation of amorphous titania and the elimination of crystal defects were completed at this temperature (Fig. 8). Moreover, the growth of the nanocrystals to an average size of 24 nm (Fig. 9) and the well-developed anatase shapes preferentially faceted with the {1 0 1} type planes were revealed, Fig. 2(g–i). HRTEM images in Fig. 2(i) and Fig. 5 confirm the high crystallinity of individual, variously oriented and well-faceted anatase single crystals possessing high photoactivity. However, since the most visible alteration of nanocrystal morphology occurred during annealing at 700 °C compared with the sample annealed at 600 °C (as seen from comparison of Figs. 8, 9 and 2(d) and (g)) it is expected that the photoactivity escalation may be predominantly related to the development of the well-faceted bipyramidal anatase nanocrystals, accompanied by the enlargement of the {1 0 1} type plane area as a result of growth in the ⟨0 0 1⟩ type directions (Fig. 2(i) and (f)).

Fig. 9. Average nanocrystal size (d) of samples annealed at 300 °C, 400 °C, 500 °C, 600 °C, and 700 °C determined by XRD method. For comparison, anatase nanocrystal size of TiO$_2$ standard Aeroxide® P25 is provided.

4. Conclusions

In summary, high-energy ball milling of the $TiOSO_4 \cdot 2H_2O$–Na_2CO_3 mixture for 5 min followed by annealing at 700 °C led to anatase nanocrystals highly efficient in photoinduced scavenging of the semi-stable DPPH radical. They exhibited high crystallinity and an average size of 24 nm. The development anatase nanocrystals was examined and the dependence of the photoactivity on the annealing temperature was closely related with crystallinity, size and the morphology.

The increment of photoactivity after annealing at 400 °C was explained by the increasing fraction of anatase nanocrystals and consuming the amorphous titania. Although crystallinity was significantly improved, the sample produced by annealing at 500 °C did not exhibit increase in photoactivity compared to sample annealed at 400 °C. This was assigned to spherical-like morphology of anatase nanocrystal. Moderate increase in photoactivity of highly crystalline anatase prepared by annealing at 600 °C was mainly attributed to partial faceting of nanocrystals by the {1 0 1} type planes. Abrupt increase in photoactivity of the sample annealed at 700 °C can be assigned to complete crystallization of the sample, optimal size, but mainly to the well developed bipyramidal morphology of anatase nanocrystals and the increment of the area fraction of {1 0 1} planes faceting these bipyramids.

The weak beam dark field (WBDF) transmission electron microscopy (TEM) method was employed to reveal the 3D morphology of anatase. Based on the thickness changes depicted in the WBDF images, it was determined that the square-like, hexagonal-like, rhomboid-like, rhombus-like, and rectangle-like shapes recorded in the BF images correspond exclusively to the tetragonal bipyramidal morphology of anatase projected along different crystallographic directions, and not to different anatase shapes. No cuboids and nanoplates/nanosheets, which are favoured by highly reactive {1 0 0} and {0 0 1} surfaces, were revealed in this sample.

The WBDF method is an invaluable tool in characterizing the 3D shape of anatase nanocrystals using TEM. To the best of our knowledge, WBDF morphological studies have not previously been used for anatase morphology determination. Therefore, we propose that this contribution may serve as a methodological guide for the more effective evaluation of the morphology and surface facets of the nanoparticulate photocatalysts under transmission electron microscopy.

References

[1] A. Mills, S.L. Hunte, J. Photochem. Photobiol. A 108 (1997) 1–35.
[2] M.A. Fox, M. Dulay, Chem. Rev. 93 (1993) 341–357.
[3] U. Gaya, A. Abdullah, J. Photochem. Photobiol. C: Photochem. Rev. 9 (2008) 1–12.
[4] A. Fujishima, X. Zhang, D.A. Tryk, Surf. Sci. Rep. 63 (2008) 515–582.
[5] A. Fujishima, T.N. Rao, D.A. Tryk, J. Photochem. Photobiol. C 1 (2000) 1–21.
[6] Q. Xiang, K. Lv, J. Yu, Appl. Catal. B: Environ. 96 (2010) 557–564.
[7] H. Kim, W. Choi, Appl. Catal. B: Environ. 69 (2007) 127–132.
[8] Z. Zhang, C. Wang, R. Zakaria, J.Y. Ying, J. Phys. Chem. B 102 (1998) 10871–10878.
[9] N. Wu, J. Wang, D.N. Tafen, H. Wang, J.G. Zheng, J.P. Lewis, X. Liu, S.S. Leonard, A. Manivannan, J. Am. Chem. Soc. 132 (2010) 6679–6685.
[10] H. Li, W. Zhang, B. Li, Wei Pan, J. Am. Ceram. Soc. 93 (2010) 2503–2506.
[11] A. Sirisuk, E. Klansorn, P. Praserthdam, Catal. Commun. 9 (2008) 1810–1814.
[12] J. Yu, Y. Su, B. Cheng, Adv. Funct. Mater. 17 (2007) 1984–1990.
[13] J. Yu, L. Zhang, B. Cheng, Y. Su, J. Phys. Chem. C 111 (2007) 10582–10589.
[14] X. Yu, S. Liu, J. Yu, Appl. Catal. B: Environ. 104 (2011) 12–20.
[15] Y. Zhao, X. Zhang, J. Zhai, L. Jiang, Z. Liu, S. Nishimoto, T. Murakami, A. Fujishima, D. Zhu, Microporous Mesoporous Mater. 116 (2008) 710–714.
[16] A. Vittaldini, A. Selloni, F.P. Rotzinger, M. Grätzel, Phys. Rev. Lett. 81 (1998) 2954–2957.
[17] A. Vittadini, M. Casarin, A. Selloni, Theor. Chem. Acc. 117 (2007) 663–671.
[18] A. Selloni, A. Vittadini, M. Gratzel, Surf. Sci. 402 (1998) 219–222.
[19] A. Tilocca, A. Selloni, J. Phys. Chem. B 108 (2004) 4743–4751.
[20] X.Q. Gong, A. Selloni, J. Phys. Chem. B 109 (2005) 19560–19562.
[21] G. Liu, J.C. Yu, G.Q.M. Luc, H.M. Cheng, Chem. Commun. 47 (2011) 6763–6783.
[22] Z. Wang, K. Lv, G. Wang, K. Deng, D. Tang, Appl. Catal. B: Environ. 100 (2010) 378–385.
[23] J.S. Chen, X. Wen Lou, Electrochem. Commun. 11 (2009) 2332–2335.
[24] S. Liu, J. Yu, M. Jaroniec, Chem. Mater. 23 (2011) 4085–4093.
[25] L. Qi, J. Yu, M. Jaroniec, Phys. Chem. Chem. Phys. 13 (2011) 8915–8923.
[26] J. Yu, L. Qi, M. Jaroniec, J. Phys. Chem. C 114 (2010) 13118–13125.
[27] K. Lv, Q. Xiang, J. Yu, Appl. Catal. B: Environ. 104 (2011) 275–281.
[28] S. Liu, J. Yu, M. Jaroniec, J. Am. Chem. Soc. 132 (2010) 11914–11916.
[29] J. Li, D. Xu, Chem. Commun. 46 (2010) 2301–2303.
[30] B. Koo, J. Park, Y. K. Kim, S.H. Choi, Y.E. Sung, T. Hyeon, J. Phys. Chem. B 110 (2006) 24318–24323.
[31] A.S. Barnard, L.A. Curtiss, Nano Lett. 5 (2005) 1261–1266.
[32] J. Pan, X. Wu, L. Wang, G. Liu, G.Q. (Max) Lu, H.M. Cheng, Chem. Commun. 47 (2011) 8361–8363.
[33] J. Yu, Q. Xiang, M. Zhou, Appl. Catal. B: Environ. 90 (2009) 595–602.
[34] X. Zhao, W. Jin, J. Cai, J. Ye, Z. Li, Y. Ma, J. Xie, L. Qi, Adv. Funct. Mater. 21 (2011) 3554–3563.
[35] W. Li, Y. Bai, W. Liu, Ch Liu, Z. Yang, X. Feng, X. Lu, K.Y. Chan, J. Mater. Chem. 21 (2011) 6718–6724.
[36] C.H. Cho, M.H. Han, D.H. Kim, D.K. Kim, Mater. Chem. Phys. 92 (2005) 104–111.
[37] F. Amano, T. Yasumoto, O.O. Prieto-Mahaney, S. Uchida, T. Shibayama, B. Ohtani, Chem. Commun. 47 (2009) 2311–2313.
[38] F. Amano, T. Yasumoto, O.O. Prieto-Mahaney, S. Uchida, T. Shibayama, Y. Terada, B. Ohtani, Top. Catal. 53 (2010) 455–461.
[39] J. Pan, G. Liu, G.Q. (Max) Lu, H.-M. Cheng, Angew. Chem. 123 (2011) 2181–2185.
[40] V. Brezova, Z. Vreckova, P. Billik, M. Caplovicova, G. Plesch, J. Photochem. Photobiol. A: Chem. 206 (2009) 177–187.
[41] M. Adachi, J. Jiu, S. Isoda, Curr. Nanosci. 3 (2007) 285–295.
[42] P.D. Christy, N. Melikechi, N.S.N. Jothi, A.R.B. Suganthi, P. Sagayaraj, J. Nanopart. Res. 12 (2010) 2875–2882.
[43] A. Chemseddine, T. Moritz, Eur. J. Inorg. Chem. 1999 (1999) 235–245.
[44] M. Posternak, A. Baldereschi, B. Delley, J. Phys. Chem. C 113 (2009) 15862–15867.
[45] T. Tachikawa, N. Wang, S. Yamashita, S.-C. Cui, T. Majima, Angew. Chem. Int. Ed. 49 (2010) 8593–8597.
[46] R.L. Penn, J.F. Banfield, Geochim. Cosmochim. Acta 63 (1999) 1549–1557.
[47] Y. Dai, C.M. Cobley, J. Zeng, Y. Sun, Y. Xia, Nano Lett. 9 (2009) 2455–2459.
[48] I. Djerdj, D. Arčon, Z. Jagličic, M. Niederber, J. Solid State Chem. 181 (2008) 1571–1581.
[49] J. Li, Y. Yu, Q. Chen, J. Li, D. Xu, Cryst. Growth Des. 10 (2010) 2111–2115.
[50] C. Perego, R. Revel, O. Duruphty, S. Cassaignon, J.-P. Jolivet, Solid State Sci. 12 (2010) 989–995.
[51] J.S. Chen, X.W. Lou, Electrochem. Commun. 11 (2009) 2332–2335.
[52] R.K. Wahi, W.W. Yu, Y. Liu, M.L. Mejia, J.C. Falkner, W. Nolte, V.L. Colvin, J. Mol. Catal. A: Chem. 242 (2005) 48–56.
[53] Y. Chen, X. He, X. Zhao, Q. Yuan, X. Gu, J. Colloid Interface Sci. 310 (2007) 171–177.
[54] T.D.N. Phan, H.-D. Pham, T.V. Cuong, E.J. Kim, S. Kim, E.W. Shin, J. Cryst. Growth 312 (2009) 79–85.
[55] N. Balász, K. Mogyorósi, D.F. Srankó, A. Pallagi, T. Alapi, A. Oszkó, A. Dombi, P. Sipos, Appl. Catal. B: Environ. 84 (2008) 356–362.
[56] Z. Ambrus, K. Mogyorósi, Á. Szalai, T. Alapi, K. Demeter, A. Dombi, P. Sipos, Appl. Catal. A 340 (2008) 153–161.
[57] R.K. Wahi, Y. Liu, J.C. Falkner, V.L. Colvin, J. Colloid Interface Sci. 302 (2006) 530–536.
[58] G.B. Shan, G.P. Demopoulos, Nanotechnology 21 (2010) 025604.
[59] B. Wu, Ch Guo, N. Zheng, Z. Xie, G.D. Stucky, J. Am. Chem. Soc. 130 (2008) 17563–17567.
[60] Y. Xu, X. Fang, Z. Zhang, Appl. Surf. Sci. 255 (2009) 8743–8749.
[61] C.T. Dinh, T.D. Nguyen, F. Kleitz, T.O. Do, ACS Nano. 3 (2009) 3737–3743.
[62] P. Billik, G. Plesch, Mater. Lett. 61 (2007) 1183–1186.
[63] P. Billik, G. Plesch, V. Brezova, L. Kuchta, M. Valko, M. Mazur, J. Phys. Chem. Solids 68 (2007) 1112–1116.
[64] C.H. Cho, D.K. Kim, D.H. Kim, J. Am. Ceram. Soc. 86 (2003) 1138–1145.
[65] A.C. Dodd, A.J. McKinely, M. Saunders, T. Tsuzuki, J. Nanopart. Res. 8 (2006) 43–51.
[66] V. Brezová, D. Dvoranová, A. Staško, Res. Chem. Intermed. 33 (2007) 251–268.
[67] V. Brezová, P. Billik, Z. Vrecková, G. Plesch, J. Mol. Catal. A 327 (2010) 101–109.
[68] J.S. Chen, C.Y. Tan, G.M. Chow, Nanotechnology 18 (2007) 435604.
[69] C.Y. Tan, J.S. Chen, B.H. Liu, G.M. Chow, J. Cryst. Growth 293 (2006) 175–185.
[70] http://www.mindat.org/min-213.html.
[71] http://www.ccp14.ac.uk/ccp/web-mirrors/weber/~weber/JAVA/jstg/jstg.html.

[72] F. Han, V.S.R. Kambala, M. Srinivasan, D. Rajarathnam, R. Naidu, Appl. Catal. A: Gen. 359 (2009) 25–40.

[73] U.G. Akpan, B.H. Hameed, J. Hazard. Mater. 170 (2009) 520–529.

[74] E.N. Hristea, M. Hillebrand, M.T. Caproiu, H. Caldararu, T. Constantinescu, A.T. Balaban, ARKIVOC Part 2 (2002) 123–132.

[75] R. Isono, T. Yoshimura, K. Esumi, J. Colloid Interface Sci. 288 (2005) 177–183.

[76] G. Dransfield, P.J. Guest, P.J. Lyth, D.J. McGarvey, T.G. Truscott, J. Photochem. Photobiol. B 59 (2000) 147–151.

[77] T.A. Egerton, J. Mattinson, J. Photochem. Photobiol. A 186 (2007) 115–120.

[78] A. Staško, V. Brezová, S. Biskupič, V. Mišík, Free Radic. Res. 41 (2007) 379–390.

[79] P. Pulišová, J. Boháček, J. Šubrt, L. Szatmáry, P. Bezdička, N. Murafa, Catal. Today 161 (2011) 84–90.